PHYSICAL REVIEW B **69**, 125316 (2004)

Nanoengineering of lateral strain modulation in quantum well heterostructures

J. Grenzer,[1,*] U. Zeimer,[2] S. A. Grigorian,[1,†] S. Feranchuk,[1,2,‡] U. Pietsch,[1] J. Fricke,[2] H. Kissel,[2]
A. Knauer,[2] and M. Weyers[2]
[1]*University of Potsdam, Institute of Physics, Am Neuen Palais 10, 14469 Potsdam, Germany*
[2]*Ferdinand-Braun-Institut für Höchstfrequenztechnik, Albert-Einstein-Strasse 11, 12489 Berlin, Germany*

(Received 5 September 2003; published 16 March 2004)

We have developed a method to design a lateral band-gap modulation in a quantum well heterostructure. The lateral strain variation is induced by patterning of a stressor layer grown on top of a single quantum well which itself is not patterned. The three-dimensional (3D) strain distribution within the lateral nanostructure is calculated using linear elasticity theory applying a finite element technique. Based on the deformation potential approach the calculated strain distribution is translated into a local variation of the band-gap energy. Using a given vertical layer structure we are able to optimize the geometrical parameters to provide a nanostructure with maximum lateral band-gap variation. Experimentally such a structure was realized by etching a surface grating into a tensile-strained InGaP stressor layer grown on top of a compressively strained InGaAs-single quantum well. The achieved 3D strain distribution and the induced band-gap variation are successfully probed by x-ray grazing incidence diffraction and low-temperature photoluminescence measurements, respectively.

DOI: 10.1103/PhysRevB.69.125316 PACS number(s): 78.55.−m, 61.10.−i, 73.21.Fg, 02.70.Bf

I. INTRODUCTION

Quantum well semiconductor heterostructures are increasingly important systems in the development of smaller, faster, and more efficient electronic and optoelectronic devices. One way to modify the electronic band structure is to exploit quantum size effects requiring device engineering on a nanometer length scale.[1] In particular, the lateral patterning of a strained stressor layer allows us to achieve a lateral carrier confinement in a buried single quantum well (SQW) as a result of the strain relaxation.[2] The strain relaxation at free surfaces of the stressor layer induces a lateral inhomogeneous strain distribution and subsequently a lateral change of the optical properties within the single SQW.

In this work, we study the influence of a patterned tensile-strained InGaP stressor layer on the optical properties of a buried compressively strained InGaAs-SQW grown on an exactly oriented (001) GaAs substrate. After patterning of the stressor the resulting strain field depends on the vertical layer sequence (i.e., In content and layer thicknesses of the SQW and the stressor) and the geometrical parameters of the surface grating such as period, ridge-to-valley ratio, and angle of valley sidewalls. These parameters have to be optimized to achieve a maximum lateral band-gap variation within the SQW.

The finite element method (FEM) is a well-established engineering technique in many areas of product design. In particular, a linear elasticity model in a FEM approach can be applied for the calculation of the three-dimensional (3D) strain distribution in semiconductor nanostructures. This was demonstrated for self-organized structures[3,4] as well as for laterally nanostructured semiconductors.[5] Using an analytical model, the influence of the elastic deformation on the optical properties of quantum wire structures was investigated theoretically[6] as well as experimentally using photoluminescence (PL) and x-ray diffraction.[7]

In the following FEM will be implemented to find structural parameters which provide a maximum lateral variation of the strain distribution and therewith of the band-gap energy. The resulting optimized parameters are used as target values for sample preparation.

The 3D strain distribution within the samples is studied by grazing incidence x-ray diffraction (GID). This method is very sensitive to thin layers due to its capability to vary the penetration depth of the probing x-ray beam. Moreover, the GID technique allows us to obtain the in-plane strain information within a surface grating structure.[8–10] The measured GID intensity profiles are simulated based on the distorted-wave Born approximation[5,11] (DWBA) using the displacement field calculated by FEM. The x-ray experiments were performed at two different synchrotron radiation facilities, i.e., at the beam line ID10B at the ESRF (Grenoble, France) and at the beam line BW2 at HASYLAB (Hamburg, Germany).

Finally, the optical properties of the InGaAs-SQW are analyzed by PL at 10 K. The measured energy shift of the PL line after lateral patterning is interpreted in terms of a deformation potential approach[12,13] where the local strain calculated by FEM is translated into a variation of the band-gap energy.

II. FINITE ELEMENT METHOD

As the main structural element of the nanostructure under investigation, we chose a 10 nm thick pseudomorphic $\mathrm{In_{0.16}Ga_{0.84}As}$-SQW with a compressive strain of -1.1% embedded between GaAs barriers. This heterostructure emits at room temperature at a wavelength of 980 nm which is an interesting wavelength for many device applications. As the stressor layer tensile-strained InGaP with variable In content and thickness was chosen. The lateral structure is made up of a surface grating etched into the InGaP stressor layer with ridges and valleys running parallel to $[1\bar{1}0]$. Figure 1 shows the general layout of such a laterally patterned nanostructure. Using suitable boundary conditions and taking into account the symmetry of the nanostructure, a single half period of the

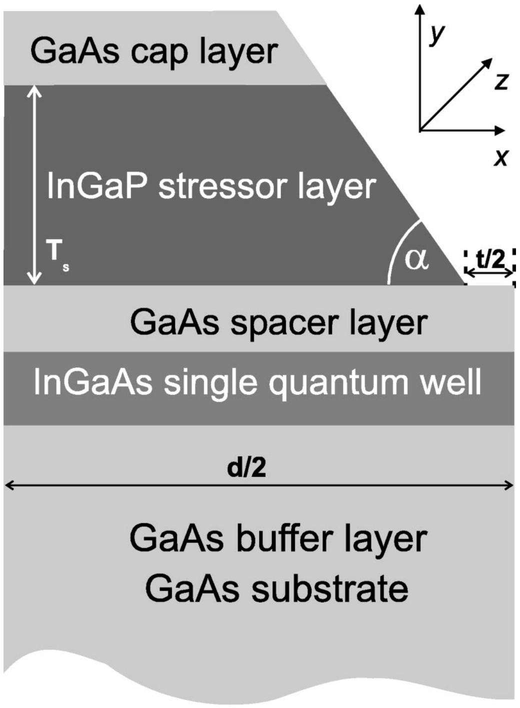

FIG. 1. Schematic layout of one half period of the laterally patterned nanostructure.

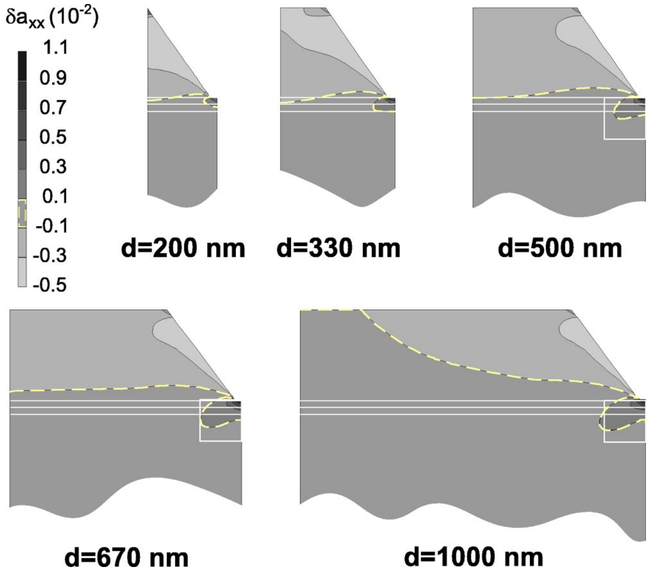

FIG. 2. FEM calculation for nanostructures with different periods, the white squares depict the positions of the high tensile-strained regions. The thin continuous lines mark the position of the SQW and the spacer layer. The thick dashed line separates the strained regions from the unstrained part of the nanostructure ($\delta a_{xx} < 0.1\%$).

nanostructure was considered for the FEM calculations. The most important parameters of this cutout are the half period $d/2$ and the half valley width $t/2$ as indicated in Fig. 1. The y axis of our laboratory system is chosen parallel to the surface normal, the z axis is directed along the valley direction, and the x axis is perpendicular to the trenches.

The stressor is initially pseudomorphic and tensile. The strain relaxation mainly appears at the free surface of the stressor ridges leading to a smaller lateral lattice constant $a_{\parallel}$ compared to that of the GaAs substrate. We used FEM to investigate the influence of different structural parameters on the strain field created within the lateral nanostructure. In particular, we changed the grating parameters d and t as well as the thicknesses of the GaAs barrier layer and of the InGaP stressor layer T_S. Additionally the amount of strain deposited in the stressor layer was varied.

The FEM analysis was carried out using the commercial software package MSC.MARC. One single half period of the nanostructure was subdivided into small parallelograms or trapezoidally shaped finite elements. Nonregular subdivisions were necessary to minimize the size of finite elements in and close to critical areas, i.e., within the SQW and at highly strained regions close to the valley edges. Our computational resources allowed to define parallelograms of 2.5 nm side length and trapezoidal-shaped finite elements with 2 nm for smallest side length, respectively.

Depending on the lateral period d and valley width t the nanostructures were subdivided into 2000 to 15 000 finite elements for the narrowest and largest lateral structures, respectively. The periodicity of the gratings was taken into account by periodic boundary conditions. For each of the small finite elements (usually consisting of eight nodes) the displacements were calculated iteratively up to a termination condition defined by the achieved minimum of strain energy of the whole system.

The program provides the distributions of the elastic strain fields ε_{mn} $(m,n=x,y,z)$ as well as of the lattice misfit $\delta a_{mn}=\Delta a/a|_{mn}$ of a given nanostructure. The strain is given by $\varepsilon_{mn}(x,y,z)=(a_{Lm}-a_{L0})/a_{L0}$, where a_{Lm} describes the lattice constant of the layer in the direction $m,n=(x,y,z)$ and a_{L0} is the relaxed cubic lattice constant of the same material.

Grazing incidence x-ray diffraction is a sensitive method to probe the lateral lattice misfit $\delta a_{xx}=(a_{Lx}-a_0)/a_0$ (a_0 is lattice constant of the substrate) for different depths below the sample surface, which monitors exactly the change of the lateral lattice constant caused by the patterning. Therefore a tensile lateral lattice misfit is defined by a lateral lattice constant of the layer a_{Lm}, which is larger than the lattice constant of the substrate a_0.[14]

For the calculation of the displacement field we used the lattice parameters and elastic constants given in Ref. 15.

Figure 2 shows the calculated lateral lattice misfit δa_{xx} for laterally patterned structures with different periods, i.e., $d=200$, 330, 500, 670, and 1000 nm, but at a fixed valley width $t=20$ nm and a stressor thickness T_S of 120 nm. The pseudomorphic strain of the stressor layer is 0.3%. Beneath the ridges the lateral lattice misfit is always weakly compressive whereas beneath the valley a high tensile lateral lattice misfit is observed. Thus, the strain varies strongly along the x axis and increases with increasing period. The lateral strain modulation starts to saturate when the period exceeds a value of $d=500$ nm. In this case the tensile lateral lattice misfit is almost identical in latitude and magnitude (see white boxes in Fig. 2). Therefore we considered nanostructures with d

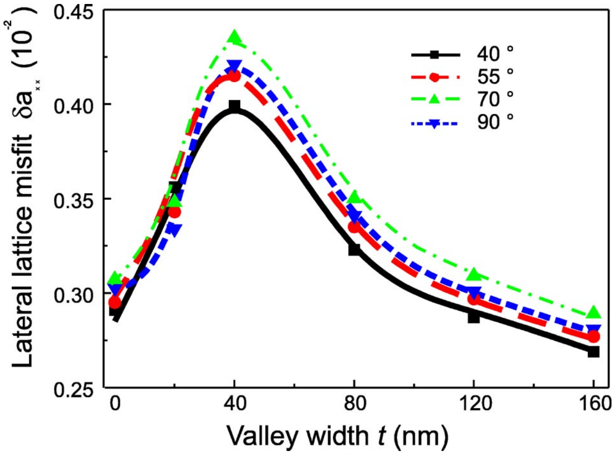

FIG. 3. Change of the maximum lateral lattice misfit δa_{xx} as a function of the valley width and the facet angle; the lines are guides for the eyes.

$=500$ nm for further optimization.

In the next step, the facet angle α (see Fig. 1) of the InGaP stressor layer was varied. The influence on the strain field was calculated changing α in a range from 40° to 90°. From the calculations it follows that the strain mainly changes with the valley width and only weakly with α. The maximum value of δa_{xx} was always found at valley width of 40 nm. Figure 3 shows the influence of the facet angle on the lateral lattice misfit δa_{xx}. The largest δa_{xx} values were found for the facet angle of 70°. However, these values are only 5% larger than those calculated for the facet angle of 55°. Therefore, we can fix α at a value of 54° which corresponds to the {111} orientation of the side facets obtained after wet chemical etching.

The influence of the valley width t and the thickness of the GaAs spacer layer on the strain distribution and the optical properties of the nanostructure will be later discussed in detail.

III. GROWTH AND PREPARATION OF THE LATERALLY PATTERNED NANOSTRUCTURE

In the preceding section we presented the general construction of the SQW heterostructure and showed how to determine the optimum geometrical parameters for maximum strain. Experimental conversion of these parameters has to consider two main technological restrictions of growth and lateral patterning. The first restriction concerns the maximum thickness of the stressor layer. As well known, pseudomorphic growth is possible up to a critical thickness. It may be possible to grow a strained layer above the critical layer thickness, however, such structure is metastable and will relax under generation of misfit dislocations. The next restriction concerns the minimum distance between two ridges. Due to technological reasons connected with the holographic photolithography used for the preparation of the surface grating (see Ref. 9), it cannot be smaller than 100 nm for a grating period of 500 nm. Considering these restrictions, using FEM a lateral nanostructure was designed to obtain a maximum lateral strain modulation.

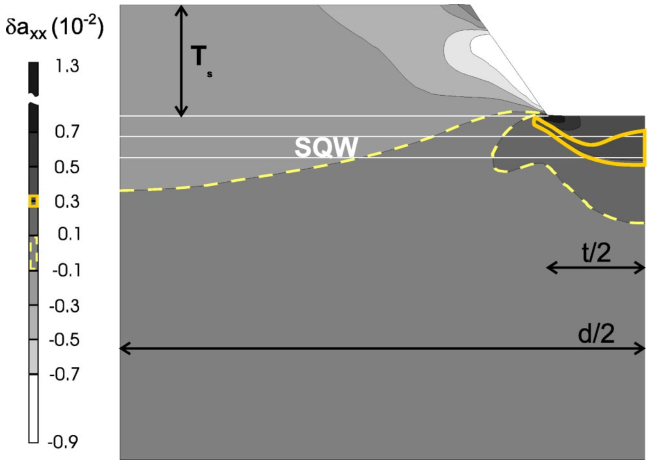

FIG. 4. Strain distribution calculated by FEM in the optimized nanostructure with the following parameters: $d=500$ nm, $t=90$ nm, $T_S=40$ nm, tensile pseudomorphic strain of the stressor layer of 0.73%; the white thin lines depict the positions of the InGaAs-SQW and the spacer layer. The thick continuous line marks a region of tensile strain between $\delta a_{xx}=0.27$ and 0.33%. The dashed line separates the strained regions from the unstrained part of the nanostructure ($\delta a_{xx}<0.1\%$).

A vertical layer structure was grown on a (001)-GaAs substrate by metalorganic vapor phase epitaxy. As mentioned above, it consists of a 10 nm thick InGaAs-SQW with an In content of 16% corresponding to a pseudomorphic compressive strain of -1.1%. The GaAs barrier and etch-stop layer had a thickness of 10 nm. Considering the predictions from FEM, subsequently a 40 nm thick InGaP stressor layer with tensile pseudomorphic strain of 0.73% was grown followed by a 10 nm thick GaAs cap layer which was necessary for technological reasons. The achieved layer parameters, such as thicknesses and compositions of the as-grown structure, were checked by high-resolution x-ray diffraction. For the lateral patterning of the stressor layer we applied holographic photolithography and, subsequently, wet chemical etching using $\mathrm{HCl{:}H_3PO_4}=3{:}1$. The GaAs cap layer and the InGaP layer were partially removed down to the GaAs etch-stop layer. The resulting surface grating had a lateral period of $d=500$ nm and a valley width of $t=90$ nm. The valley sidewall facets became {111} oriented.

Figure 4 shows the result of the FEM calculation for the sample described above. The relaxation of the nanostructured stressor layer leads to a reduction of its lattice constant; the resulting average lateral lattice misfit (of the stressor layer) gives a value of $\delta a_{xx}\approx-0.3\%$. The relaxation of the stressor induces an additional tensile lateral lattice misfit into the volume beneath the valley with lateral and vertical lengths of about 100×50 nm^2. The lattice misfit in the region of the SQW (marked by a thick continuous line) amounts to a value in the range of $\delta a_{xx}=0.27$–0.33%.

IV. GRAZING INCIDENCE DIFFRACTION

The GID experiment was carried out to verify the calculated 3D strain profile of the nanostructure. A schematic lay-

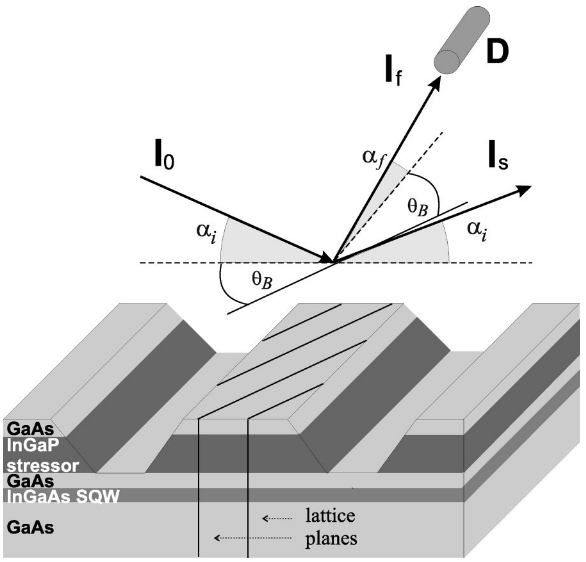

FIG. 5. Experimental GID setup.

out of the experimental setup is shown in Fig. 5. The incident beam strikes the sample surface at an incidence angle α_i, which was changed from 0.08° to 0.4°. The crystal is rotated around the surface normal to excite the (220) reflection at an in-plane scattering angle $\theta = \theta_B$. The diffracted beam was analyzed at an exit angle α_f. The beam energy was 10 keV.

Any lateral periodicity of strain provides grating peaks appearing as subsidiary intensity maxima close to an in-plane Bragg peak. These are probed at a penetration depth L_{pen} which depends on α_i. If α_i is smaller than the critical angle of total external reflection α_c, the incoming beam becomes evanescent and propagates parallel to and close below the surface. In this case L_{pen} is restricted to several nanometers only. However, by increasing α_i the penetration depth increases to several hundred nanometers ($\alpha_i > \alpha_c \sim 27°$). One advantage of the GID geometry is the possibility to separate the influence of strain and shape from the intensity profiles using two equivalent Bragg reflections. For the transverse scans across the $(2\bar{2}0)$ Bragg reflection grating peaks appear only due to periodicity of the chemical composition of the nanostructure, which is similar to a lateral modulation of the electron density. In this scan the length of the scattering vector is kept constant $\mathbf{Q} = \sqrt{8}\pi/a_0(\mathbf{H},\mathbf{K},\mathbf{L})$ (a_0 is the GaAs lattice parameter, and $\mathbf{H} \| [110]$, $\mathbf{K} \| [1\bar{1}0]$, $\mathbf{L} \| [001]$). On the other hand, longitudinal scans across the (220) Bragg reflection, where the length of the scattering vector $\mathbf{Q}$ changes, are additionally sensitive to the influence of the lateral lattice misfit.[5]

The GID curves were simulated using the DWBA approach,[5,11] which is valid for nanostructures with any material composition and geometrical configuration including a surface grating. Following the DWBA approach, we describe the effects connected with the propagation of the incident wave exactly dynamically (i.e., reflection, transmission, refraction, and absorption in the surface layers and GaAs substrate). All other scattering effects, especially diffraction effects, are treated kinematically. Taking into account the transmitted reflected wave and the diffracted one, the coherently scattered intensity of diffracted waves can be calculated. As an input for the summation of scattered amplitudes we use the initial positions for all nodes and their displacements generated by FEM calculation. Our GID simulation is restricted to a coherent scattering process and we did not take into account diffuse scattering, which is caused by lattice and SQW imperfections. Each small finite element is considered to be uniformly strained and diffracts at a Bragg position which is determined by the local strain. The x-ray simulation provides the intensities of the grating peaks only, which in case of a longitudinal scan corresponds to the Fourier transform of the strain distribution of the nanostructure (see, e.g., Refs.[11,16]). Due to the kinematic scattering our model fails for the description of the substrate Bragg peak, especially for large penetration depths. By this reason, the substrate peak appears for larger α_i more intense in simulation than in the experiment.

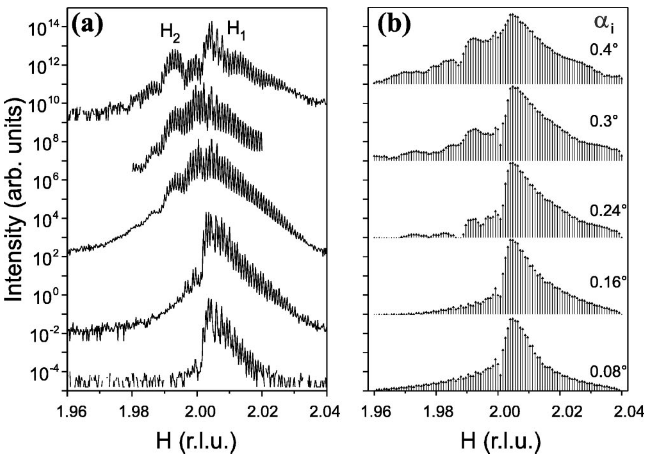

FIG. 6. Experimental (a) and calculated (b) GID pattern (longitudinal scans) as a function of the angle of incidence α_i.

Figure 6 shows experimental GID data (a) and results of the calculations (b) of the GID intensity profiles of the longitudinal (220) reflection as a function of the incidence angle α_i. The sample is the one described in the preceding section. The inhomogeneous strain field creates an asymmetrical intensity profile, the shape of which depends on $L_{pen}(\alpha_i)$. Due to relaxation of the InGaP stressor layer the compressive lateral lattice misfit at the ridge positions calculated by FEM becomes qualitatively visible by a shift of the intensity maximum out of the position of the GaAs substrate reflection $H_0 = 2$. For all α_i the main intensity maximum is shifted to $H_1 > 2$. The main peaks of the simulated and experimental curves are located at $H_1 \simeq 2.005$ and allow us to calculate the lateral lattice misfit from $(H_1 - H_0)/H_0 = -\delta a_{xx}$, which equals $\delta a_{xx} = -0.25\%$. This value corresponds to the average lateral lattice misfit of the relaxed InGaP stressor layer as shown in Fig. 4. The substrate reflection becomes visible at a larger incident angle $\alpha_i = 0.4°$.

With increasing penetration depth of the x-ray beam an additional local intensity maximum appears at $H_2 < 2$ (see Fig. 6), indicating a region with tensile lateral lattice misfit. These highly strained regions are located beneath the valleys (dark colors in Fig. 4). An averaged lateral lattice misfit of $\delta a_{xx} = 0.33\%$ was extracted from the x-ray data. This coincides with the FEM calculation where a value of about 0.3% was found for the strain in the SQW itself (thick continuous line in Fig. 4). Thus, the agreement between experiment and simulation is sufficiently good. The remaining discrepancies might be caused by the limited number of finite elements considered in the regions of large strain gradients and the restrictions of the DWBA approach.

A general approach to translate the calculated strain distribution within the nanostructure into a local change of a photoemission line is presented in the following section.

V. INFLUENCE OF STRAIN ON THE LATERAL BAND STRUCTURE

Optical transitions in semiconductor quantum wells are usually studied by photoluminescence. The PL spectra can be used to characterize the change of the band structure under the influence of an applied strain. The deformation potential approach[12,13] provides a relation between an applied strain and the change of electronic band edges of a semiconductor. In the present case, the displacement field created by FEM was used to calculate the strain tensor of a particular finite element which was than translated into a local change of the band edges. The strain-induced shift of the PL line is given by

$$\Delta E(x,y)=\Delta E_s^c(\varepsilon_{mm}(x,y))+\Delta E_q^c(t_x,t_y)+\Delta E_s^v(\varepsilon_{mn}(x,y))+\Delta E_q^v(t_x,t_y), \tag{1}$$

where $\Delta E_s^c(\varepsilon_{mm}(x,y))$ and $\Delta E_s^v(\varepsilon_{mn}(x,y))$ are the strain-induced shifts of the conduction- and valence-band edges at the spatial position (x,y), and $\Delta E_q^c(t_x,t_y)$ and $\Delta E_q^v(t_x,t_y)$ are the energy shifts caused by the change of the lateral (t_x) and the vertical (t_y) quantizations. The strain and quantization terms contribute with opposite sign to the total energy shift. An increase of lateral quantization energy takes place for decreasing t_x and causes an increasing blue shift whereas, in our case, the lateral strain relaxation of the ridges leads to a red shift. Because the exciton binding energy and the effective masses of the constituents depend only weakly on a strain variation, we will not consider these dependencies. Following Ref. 15, the offset of the conduction band was set to 0.75. Note that there is no strain variation along the z axis; i.e., along the ridges and valleys.

Considering a compressively strained SQW, the heavy- and light-hole bands are split at the Γ point and the heavy hole band is the highest valence band. For the unpatterned sample we have a rectangular quantum well with a barrier height of about 120 meV for the electrons and 30 meV for the heavy holes. Following Ref. 17 the first energy quantization levels in the SQW were estimated to be 29 meV and 6 meV, respectively.

Figure 7 displays the band structure of a patterned sample for a single period (upper right structure in Fig. 2; $d=500$ nm, $t=20$ nm, $T_S=120$ nm, with a pseudomorphic strain of 0.3%). It is shown that the strain modification of the band edges is much stronger for the conduction band compared to the valence band. Not only the SQW (straight line) is affected by the lateral strain modulation, but also the GaAs barrier layers embedding the SQW. The 10 nm thick GaAs barrier layer which acts additionally as etch-stop layer for the stressor (dotted lines) exhibits in particular a stronger dependence on strain due to its close proximity to the stressor layer. Fortunately, the amount of elastic moduli and deformation potential constants of the constituents are very similar. The barrier height for electrons is almost constant with a reduction of only 10 meV at the valley edges. The hole barriers exhibit a similar behavior. Since for the unpatterned sample the barrier height for the electrons amounts to 120 meV, the vertical quantization levels are almost not affected by the induced strain as long as the change of the barrier height is less than 10%. Therefore in most cases one can calculate the strain-induced shift of the SQW band edges with the assumption that the vertical quantization does not change with the lateral strain modulation.

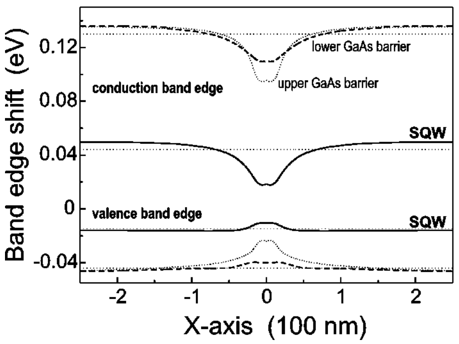

FIG. 7. Calculation of the conduction and valence bands for the InGaAs-SQW (straight lines) and the GaAs beneath (dashed line) and above it (dotted line) using the displacements from FEM calculations of the upper right structure of Fig. 2 (band edges for the unpatterned sample are indicated as thin dotted lines).

Under these circumstances, a PL energy shift is mainly caused by the strain-induced change of the band gap ΔE_s:

$$\Delta E_s(x,y)=\Delta E_s^c(\varepsilon_{mn}(x,y))-\Delta E_s^v(\varepsilon_{mn}(x,y)), \tag{2}$$

where ΔE_s^c and ΔE_s^v are the energy shifts of conduction and valence bands, respectively. The effect of strain on the band edges can be written as

$$\Delta E_s^c(x,y)=a_c(\varepsilon_{xx}+\varepsilon_{yy}+\varepsilon_{zz}), \tag{3}$$

$$\Delta E_s^v(x,y)=a_v(\varepsilon_{xx}+\varepsilon_{yy}+\varepsilon_{zz})\pm\left[\frac{b^2}{4}(\varepsilon_{xx}-2\varepsilon_{yy}+\varepsilon_{zz})^2+\frac{d^2}{4}[4\varepsilon_{xy}^2+(\varepsilon_{xx}-\varepsilon_{zz})^2]\right]^{1/2}. \tag{4}$$

Here a_c and a_v are the hydrostatic deformation potential constants for the conduction and valence bands, and ε_{mn} $(m,n=x,y,z)$ are the components of the elastic strain tensor depending on the spatial coordinates x and y. The shear deformation potential constants b and d induce the splitting of the valence band. The positive sign in Eq. (4) corresponds to the heavy holes and the negative one refers to the light holes. The shear deformation affects mainly the valence-band edges of the GaAs spacer layer.

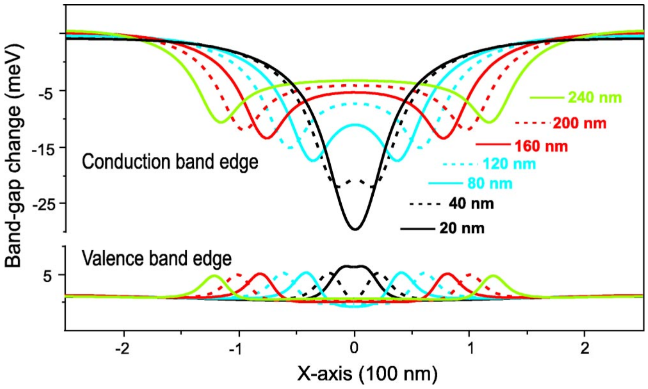

FIG. 8. Conduction- and valence-band edge change as a function of valley width.

Equations (3) and (4) were obtained using the general approach of Pikus and Bir taking into account our laboratory coordinate system mentioned above.[12] The main assumption of our approach is to apply these formulas to each of the calculated finite elements and to calculate their band splitting as a function of local strain. This approach has been successfully applied for the calculation of PL emission lines from free standing and buried SQW's in lateral nanostructures defined by wet chemical etching.[18]

A very similar sample with a band structure as shown in Fig. 7 was already investigated in Ref. 19. Here a red shift of 26 meV of the PL line was found. This experimental value is in good agreement with an estimate following Eqs. (3) and (4), where a value of 28 meV was determined.

Figure 8 shows the calculated strain-induced shifts of the conduction- and valence-band edges as functions of the x coordinate for different valley widths (see Fig. 2) using a stressor thickness of 120 nm and a pseudomorphic strain of 0.3% as before. The band-edge shifts were calculated using Eqs. (3) and (4) for structures with a period of $d=500$ nm and valley widths varying between $t=20$ nm and $t=240$ nm.

The strain-induced band-edge shift decreases for increasing t. The maximum of the band-edge shift always appears in regions of maximum tensile lateral lattice misfit located close to the edges of valleys (see Fig. 2). It reaches a maximum value for a nearly triangular shape, i.e., for $t<20$ nm. Note that this value is considerably smaller than the valley width of 40 nm, where the lateral lattice misfit δa_{xx} has its maximum (see Fig. 3). According to Eqs. (3) and (4) the band-edge shifts are mainly defined by the trace of the elastical strain tensor ε_{mn} and not only by one component.

For increasing t the strongly strained regions move out to larger $|x|$ and have a smaller maximum strain. This is accompanied by a decrease of the band-edge shift at $x=0$ as well as by the occurrence of a double-valley-like potential for the carriers. The largest band-edge shift will be obtained if the regions of maximum strain overlap, i.e., when t is smaller than 40 nm. Following Eq. (1), the achievable band-gap shift by strain is then limited by the increasing influence of lateral quantization. This effect becomes important when the lateral extension of the highly strained region is much smaller than 40 nm. Therefore, for larger t we have neglected this effect in our calculations, but it has to be considered in any case if the lateral size of a local band-edge minimum becomes smaller than 20 nm and the respective conduction-band-edge shift is larger than 10 meV.

Assuming that our approach of the spatially resolved translation of strain into band-edge energy is correct and the thermal activation energy for the carriers is smaller than the induced band-edge shift, the optically excited electrons and holes will primarily recombine at spatial positions with a minimum band gap. In the present structure most of the electrons accumulate beneath the valleys and can only diffuse along the $[1\overline{1}0]$ direction (z direction), while the potential barrier near the valley edges prevents a diffusion out of the valley region. A similar barrier exists for the valence band. Due to the limited carrier diffusion length some electrons and holes can recombine as well below the ridges, but the intensity of this transition should be much lower. Under these circumstances the electron-hole recombination takes place at two spatially separated positions, namely, beneath the valleys and beneath the ridges, generating two spectrally distinct electronic transitions. The existence of such a lateral carrier confinement was verified by scanning near-field microscopy.[20]

We calculated the gap energy shift as a function of the upper GaAs barrier layer thicknesses, namely, for 5 nm and 10 nm thick layers. The maxima of the energy-band-edge shifts were found at the same t values. Since the sum of thicknesses of the SQW and the GaAs barrier is smaller than the vertical dimension of the strained volume beneath the valley, the energy shift does not change significantly with the GaAs barrier layer thickness. Therefore, we have chosen a 10 nm thick barrier to ensue the selective etching of the trenches.

Next, we varied the thickness of the InGaP stressor layer T_S in a range from 40 nm to 200 nm, keeping all other parameters fixed. A saturation was found for both the generated lateral strain amplitude and the band-gap shift for $T_S>120$ nm. Moreover, our FEM calculations provide a certain relation between the stressor thickness T_S and the created strain acting on the underlying material. For a given pseudomorphic strain of the stressor one always finds a certain T_S which creates a maximum of strain within the underlying material. In other words, in order to generate a certain strain in the SQW using a smaller pseudomorphic strain (lower In content within the stressor layer) one has to grow a larger stressor thickness and vice versa. A further increase of T_S beyond the optimum does not increase the strain significantly.

VI. PHOTOLUMINESCENCE ANALYSIS

Far-field PL spectra were recorded at 10 K using a HeNe laser with an incident power of 0.4 mW as excitation source, focused down to a spot with a diameter of 0.2 mm. Figure 9(a) shows the PL spectra recorded for the patterned and unpatterned structures of the sample described in Fig. 4. The dotted line shows the PL spectrum from the sample before patterning, exhibiting a single emission peak at 1.342 eV as expected for an In content of $x=0.16$ in a pseudomorphically

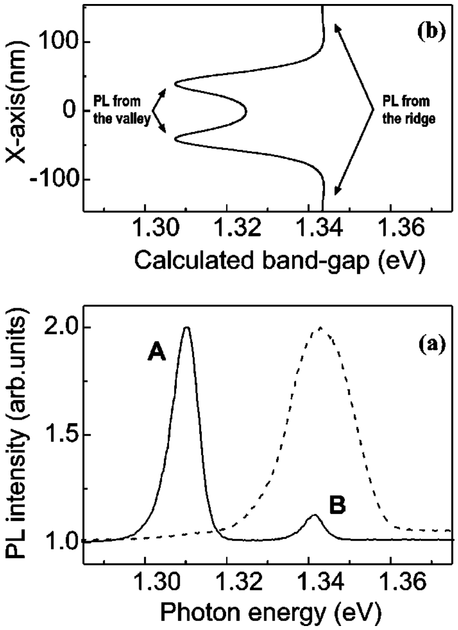

FIG. 9. Low-temperature PL spectra measured at $T=10$ K (a) of the nonpatterned nanostructure (dashed line) and of the optimized nanostructure (continuous line). The PL peak A results from the valley and peak B from the ridge, which corresponds to the nonpatterned nanostructure. (b) shows the calculated band gap for the optimized nanostructure.

strained SQW of 10 nm thickness. The full width at half maximum (FWHM) amounts to 15 meV. This relatively large FWHM is probably caused by fluctuations of the alloy composition within the InGaP layer on a nanometer length scale as identified by transmission electron microscopy. After patterning, two peaks are resolved (straight line): peak A at lower energy (1.310 eV) and peak B at higher energy (1.341 eV) but with a lower intensity. Peak A corresponds to the band gap of the strained region at the valley edges and close to it. Peak B stems from the carriers generated close to the center of the ridges. An experimental energy difference of 33 meV between the two peaks is observed. The PL energy shift [Fig. 9(b)] was calculated using the strain distribution and Eqs. (3) and (4) taking into account the first vertical quantization levels for the electrons and holes as well as the lateral quantization. The latter one is due to two minima at the edges of the valleys (see Fig. 4) and amounts to about 4 meV for electrons. Under the given assumptions, the calculated PL energy shift equals to 31 meV taking into account the calculated band-gap shift of 35 meV. The rather good agreement with the measurement ($\Delta E=33$ meV) confirms the correctness of the FEM calculation and the validity of our approach to model the strain-induced band-edge variation.

VII. CONCLUSIONS

In this paper we have shown that a lateral patterning of an initially pseudomorphically strained InGaP stressor layer results in a lateral periodic strain field, which extends towards the underlying InGaAs-SQW. The initiated lateral periodicity of the strain field causes periodic band-gap variations leading to a periodic carrier confinement. We have shown that the strain distribution calculated by FEM can be used successfully as an input to the simulation of GID x-ray diffraction curves as well as for PL energy shift calculations. The correctness of the calculated strain fields is verified independently by the good agreement between both GID and PL experimental results and calculations. The results of the GID and PL measurements confirm that a lateral periodic variation of the band gap and thus a lateral carrier confinement has been achieved which has the potential for different kinds of device applications. The obtained results allow us to predict structural and optoelectronic properties of nanostructures by FEM strain calculations, which allows us to probe design alternatives. Thus, the nanostructures can be optimized and technological efforts can be reduced.

ACKNOWLEDGMENTS

This project was supported by Deutsche Forschungsgemeinschaft (Grant No. Pi 217/18 and Grant No. Tr 357/4). The authors like to acknowledge the support of S. Konovalov and B. Struth with the GID measurements at ID 10B of the European Synchrotron Facility in Grenoble.

---

*Email address: grenzer@rz.uni-potsdam.de

†On leave from Institute of Crystallography RAS, Leninsky pr. 59, 117333 Moscow, Russia.

‡Permanent address: Belarussian State University, F. Skaryna prosp. 4/1, 220050 Minsk, Belarus.

[1] D. Bimberg, M. Grundmann, and N. N. Ledentsov, *Quantum Dot Heterostructures* (Wiley, Chichester, 1998), p. 328.

[2] K. Kash, J. M. Worlock, M. D. Sturge, P. Grabbe, J. P. Harbinson, A. Scherer, and P. S. Lin, Appl. Phys. Lett. **53**, 782 (1988).

[3] M. Schmidbauer, Th. Wiebach, H. Raidt, M. Hanke, H. Wawra, and R. Köhler, Phys. Rev. B **58**, 10 523 (1998).

[4] T. Roch, V. Holy, A. Hesse, J. Stangl, T. Fromherz, G. Bauer, T. H. Metzger, and S. Ferrer, Phys. Rev. B **65**, 245324 (2002).

[5] A. Ulyanenkov, N. Darowski, J. Grenzer, U. Pietsch, K. H. Wang, and A. Forchel, Phys. Rev. B **60**, 16 701 (1999).

[6] L. De Caro, L. Tapfer, and A. Giuffrida, Phys. Rev. B **54**, 10 575 (1996).

[7] Q. Shen, S. W. Kycia, E. S. Tentarelli, W. J. Schaff, and L. F. Eastman, Phys. Rev. B **54**, 16 381 (1996).

[8] N. Darowski, K. Paschke, U. Pietsch, K. H. Wang, A. Forchel, D. Lübbert, and T. Baumbach, Physica B **248**, 104 (1998).

[9] U. Zeimer, J. Grenzer, U. Pietsch, S. Gramlich, F. Bugge, V. Smirnitzki, M. Weyers, and G. Tränkle, J. Phys. D **34**, 183 (2001).

[10] J. Grenzer, N. Darowski, U. Pietsch, A. Daniel, S. Renon, J. P. Reithmaier, and A. Forchel, Appl. Phys. Lett. **77**, 4277 (2000).

[11] G. T. Baumbach, S. Tixier, U. Pietsch, and V. Holy, Phys. Rev. B **51**, 16 848 (1995).

[12] G. Bir and M. Pikus, *Symmetry and Strain-Induced Effects in Semiconductors* (Wiley, Chichester, 1974), p. 484.

[13] M. Grundmann, O. Stier, and D. Bimberg, Phys. Rev. B **50**, 14 187 (1994).

[14] J. W. Matthews, *Coherent Interfaces and Misfit Dislocations in*

Epitaxial Growth, edited by J. W. Matthews (Academic, New York, 1975).

[15] *Semiconductors—Basic Data*, edited by O. Madelung, 2nd ed. (Springer, Berlin, 1996), See, http://www.ioffe.rssi.ru/SVA/NSM/

[16] A. Ulyanenkov, T. Baumbach, N. Darowski, U. Pietsch, K. H. Wang, A. Forchel, and T. Wiebach, J. Appl. Phys. **85**, 1524 (1999).

[17] C. Weisbuch and B. Vinter, *Quantum Semiconductor Structures* (Academic Press, London, 1991).

[18] U. Pietsch, N. Darowski, A. Ulyanenkov, J. Grenzer, K. H. Wang, and A. Forchel, Physica B **283**, 92 (2000).

[19] U. Zeimer, J. Grenzer, S. A. Grigorian, J. Fricke, S. Gramlich, F. Bugge, U. Pietsch, M. Weyers, and G. Tränkle, Phys. Status Solidi A **195**, 178 (2003).

[20] U. Zeimer, F. Bugge, S. Gramlich, V. Smirnitski, M. Weyers, G. Tränkle, J. Grenzer, U. Pietsch, G. Cassabois, V. Emiliani, and Ch. Lienau, Appl. Phys. Lett. **79**, 1611 (2001).